Trailing edge serrations effects on the aerodynamic performance of a NACA 643418

Llorente, Elena; Ragni, Daniele

DOI
10.1002/we.2293

Publication date
2019

Document Version
Final published version

Published in
Wind Energy

Received: 28 December 2017 | Revised: 4 September 2018 | Accepted: 9 October 2018
DOI: 10.1002/we.2293

WILEY

RESEARCH ARTICLE

Trailing edge serrations effects on the aerodynamic performance of a NACA 64_3418

Elena Llorente[1] | Daniele Ragni[2]

[1]ACCIONA Windpower, Sarriguren, Spain
[2]Delft University of Technology, Delft, the Netherlands

Correspondence
Elena Llorente, ACCIONA Windpower, Sarriguren, Spain.
Email: ellorente@nordex-online.com

Abstract

A study of the aerodynamic performance of a NACA 64_3418 airfoil with trailing edge serrations is presented. For the prediction of the changes in lift due to the serration installation, an empirical law is derived that can be extended to typical cambered airfoils for wind turbine applications. The law is deduced from 2D and 3D Reynolds-averaged Navier–Stokes simulations (RANS) of the flow over the airfoil. Lift and drag together with the changes in the wake flow due to the presence of the serrated edges are investigated. An additional study of the sensitivity of the results at $Re_c = 3 \cdot 10^6$ with respect to the turbulence modeling is carried out by using three different RANS models: Spalart–Allmaras, k-omega SST, and Transition SST. Results show that the changes in lift due to trailing-edge extensions are approximated by the effect of a split plate with reduced length.

KEYWORDS

aerodynamic performance, drag, lift, reynolds-averaged navier-stokes simulations, trailing-edge serrations

1 | INTRODUCTION

In the last decade, wind turbine noise has become one of the main deterrents to the growth of new machines close to populated areas, as well as one of the major reason of annoyance for users of wind energy.[1] Wind turbine noise is mainly produced by the interaction of the blade edge with the incoming wind. The main sources of noise are divided into inflow turbulence-noise and airfoil self-noise.[2] The inflow contribution is determined by the interaction of the blade with the turbulent flow structures of the incoming flow (ie, atmospheric or wind turbulence), while the self-noise component is usually referred to as the one created by the interaction of the boundary layer of the blade with its trailing edge. In wind turbines, the contribution resulting from the passage of a turbulent boundary layer over the trailing edge is the dominant one.[3,4] A considerable amount of research has been dedicated to the reduction of trailing-edge noise using passive mitigation devices such as for example, serrated trailing edges,[5-8] porous surfaces,[9,10] and brushes.[11]

Serrated trailing edges have become recently very popular in industrial applications, because of their simple manufacturing, installation, and maintenance. These three factors give a clear advantage to serrations with respect to other solutions, either too complex or requiring additional mechanical actuation. While the efficacy of these devices in reducing noise has already been assessed by many studies (eg[8]), the change in performance due to the physical installation of these add-ons is not enough publicly documented.

This approach has been widely adopted mainly because of the possibility of retrofitting machines that are already operational with "ad hoc" tuning of the operational regimes for noise regulations limits. However, modern wind turbine blades have already largely surpassed radii of 50 m.[12,13] With such large dimensions, the blade geometry has to be developed from the design phase taking into account both aerodynamic and aeroacoustic requirements. In the last decade, researchers have decided to focus their studies on the understanding of the physical mechanism of the noise reduction, before looking into the change in performance because of the installation of the device. The study from Moreau et al,[5] for example, analyzed the noise reduction mechanism of sawtooth trailing-edge serrations on a flat plate at low to moderate Reynolds number. Besides, a 3 dB reduction of the broadband noise levels at low frequencies were measured, and a significant attenuation (of up to 13 dB) of blunt vortex-shedding noise at high frequencies without modifying the directivity of the radiated noise was achieved. Several others populate the

panorama of studies on the noise attenuation capabilities of these geometries, as for example, Gruber et al,[7] which performed wind tunnel tests for over 30 sawtooth geometries on a NACA 65(12)-10 airfoil, obtaining noise reductions between 4 and 6 dB in all test cases. Other experimental investigations on trailing edge serrations focused on full scale applications of wind turbine blades: Oerlemans et al[8] tested, for example, serrated trailing edge extensions in a real-wind turbine of 94 m of rotor diameter and obtained noise reductions of 3.2 dB due to these passive devices.

When comparing the availability of information about the effectiveness of these devices with the needs to actually predict their impact on the blade performance, few works are targeting the design of serrations, which, on the other side, often show neutral or even positive effects on the total turbine load. One of the main reasons for this imbalance lays in the large variety of profiles used by industrial manufacturers, which makes the scaling with respect to the blade shape extremely challenging. One of the most interesting works concerning the aerodynamic impact of serrations is presented by Liu et al,[14] who performed experimental tests on symmetric and asymmetric airfoils with different serrated trailing edges. In their work, the authors showed that the installation of trailing edge serrations can significantly change the aerodynamic performance of the airfoil. A second reason that might justify the relatively low abundance of studies upon the aerodynamic aspects of serrations can be attributed to the substantial complexity of their flow. Recent experimental and computational investigations, in fact, (eg other studies[15-18]) have shown that the flow over the serrated trailing edge is rather complex. Computational studies carried out by Jones et al[15,18] from direct numerical simulations on a symmetric airfoil (NACA0012) with add-ons have been highlighting the positive effects that serrations have shown in breaking up the turbulent structures convecting into the wake, especially through the development of extra horseshoe vortices originating at the serration location.

In this manuscript, a detailed numerical study of the aerodynamic performance of trailing-edge serrations together with their installation effects is performed for a NACA 64_3418 airfoil at high-Reynolds number ($Re_c = 3 \cdot 10^6$). Two- and three-dimensional simulations are carried out with the intent of quantifying the change of aerodynamic performance because of serrations. A comparison between the 2D simulations of the airfoil (with and without trailing-edge extensions) and the 3D ones is accomplished to derive an approximation of the aerodynamic characteristics based on a simplified model. Installation effects by simulating different plate thicknesses have been performed comparing 2D simulations for the three different turbulence models. The analysis is then extended to the influence of the flap angle (angle between the chord of the airfoil and the installed add-ons) carried out in the second section of the results, just 2D simulations have been performed. Three different flap angles between 2.5° and 10° have been simulated with the aforementioned turbulence models. In the last two sections of the results, a complete analysis of the flow statistics around the trailing-edge extensions has been performed together with a comparison between the aerodynamic coefficients for the three different turbulence models. Three-dimensional simulations of the clean airfoil with a straight edge, the airfoil with a split plate, and the airfoil with a serrated trailing edge have been carried out. For these geometries, aerodynamic coefficients have been studied, and an analysis of the influence of the results with respect to turbulence viscosity-ratio and turbulence intensity has been included. The results are finally used to derive a numerical law for the prediction of the change in lift and drag because of installation of serrations in a family of NACA six-digit airfoils.

2 | COMPUTATIONAL TEST CASE

The computational test case employs a NACA 64_3418 airfoil. The profile is typically used in wind turbine blades at $Re_c > 1 \cdot 10^6$.[19] The trailing edge of the original airfoil profile has been modified from sharp to a thickness of 0.2% of the chord, which corresponds to a conventional measure for airfoils of about 1.5 m chord found at a radius of about 75% of the blade length in 3 MW machines. The airfoil has been first simulated in a 2D configuration with a chord (c) of 1 m and subsequently extruded into a 3D wing. Serrated trailing edges have been modeled by periodic inserts of length of $2h = 0.187$ c and amplitude of $\lambda = 0.140$ c as shown in Figure 1. The values correspond to the ones found in literature in the work of Gruber et al[7] providing with about 5 dB of noise reduction (at a Reynolds number of 413.000).

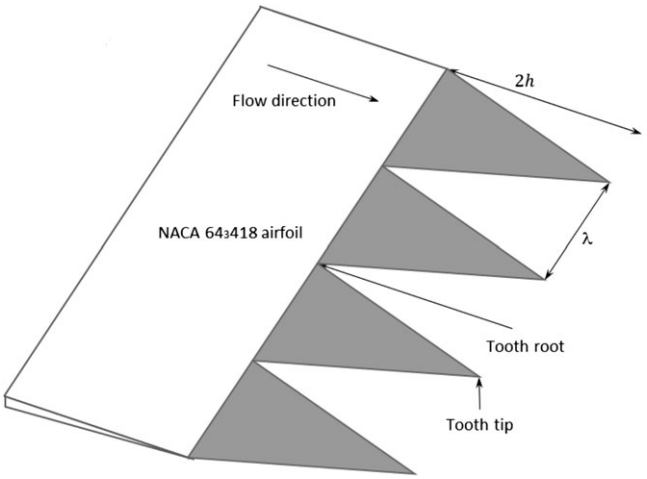

FIGURE 1 Serrations extensions with length of 2h and amplitude of λ

In the 2D simulations, the effect of the serrated trailing edge has been modeled by a split plate. In the original configuration, the simulations have been carried out with a split plate having the same length and flap angle of the serration geometry. The noise reduction has been found increasing as λ is reduced. A relation between serration length and amplitude of $\frac{\lambda}{2h} = 0.75$ is reported suitable to obtain a good noise reduction in the mid-frequency range with small-noise penalties in the high one. A first study has been carried out with a flat-plate length equal to the serration one (0.187 c) and a flap angle of 5°. An analysis of the flap angle has also been performed. Three different flap angles have been calculated: 2.5°, 5°, and 10°. Figure 2 shows the different geometries simulated, with and without trailing edge extensions.

The sensitivity of 2D and 3D simulations to the modeling of turbulence has been assessed by studying the changes of loading with respect to different turbulence models. The chosen models for the present studies vary from the most simple Spalart–Allmaras one, to the k-omega SST, and the Transition SST ones. The one-equation Spalart–Allmaras model solves the modeled transport equation for the kinematic eddy turbulent viscosity.[20] This model was originally designed for aerospace applications involving wall-bounded flows, and it showed good results for boundary layers subjected to adverse pressure gradients. The Spalart–Allmaras model was developed for aerodynamic flows, and it suffers in the correct reproduction of free shear flows, especially plane and round jet flows. In addition, it is relatively inaccurate in the prediction of homogeneous, isotropic turbulence. The main advantages are its robustness, fast convergence, and computational time.

The k-omega shear stress transport (SST) model is a two-equation eddy-viscosity model with the feature of being able to represent the k-epsilon characteristics in the freestream, and, thereby, avoiding the reported k-omega sensitivity of the solution to the inlet freestream turbulence properties. One of the main reported features of the k-omega formulation is the possibility to use it in the inner parts of the boundary layer (absence of damping functions at the wall, due to the turbulent cascade modeling via omega) features, which makes the model quite reliable in the prediction of developing boundary layers. Menter[21] demonstrates that the SST model shows a better agreement with experimental data for adverse pressure boundary layer flows than the original k-omega model of Wilcox. The k-omega SST model modifies the turbulent viscosity definition to account for the transport of the principal turbulent shear stress. This feature gives the SST k-omega model an advantage in terms of performance over both the standard k-omega model and the standard k-epsilon model. Other modifications include the addition of a cross-diffusion term in the omega equation and a blending function to ensure that the model equations behave appropriately in both the near-wall and far-field zones.

The transition SST model is based on the coupling of the SST transport equations with two other transport equations, one for the intermittency and one for the transition onset criteria, in terms of momentum-thickness Reynolds number. This model was developed by Menter et al[22] to improve how among many parameters, the freestream turbulence, pressure gradients, and turbulent length scale affect the transition of the boundary layer to turbulent flow.

In the present test cases, an inflow condition with low turbulence has been imposed in the far field. The incoming flow conditions have been uniformly set for all the models with equivalent parameters to obtain a turbulent intensity of 0.1% of the freestream and a turbulent viscosity

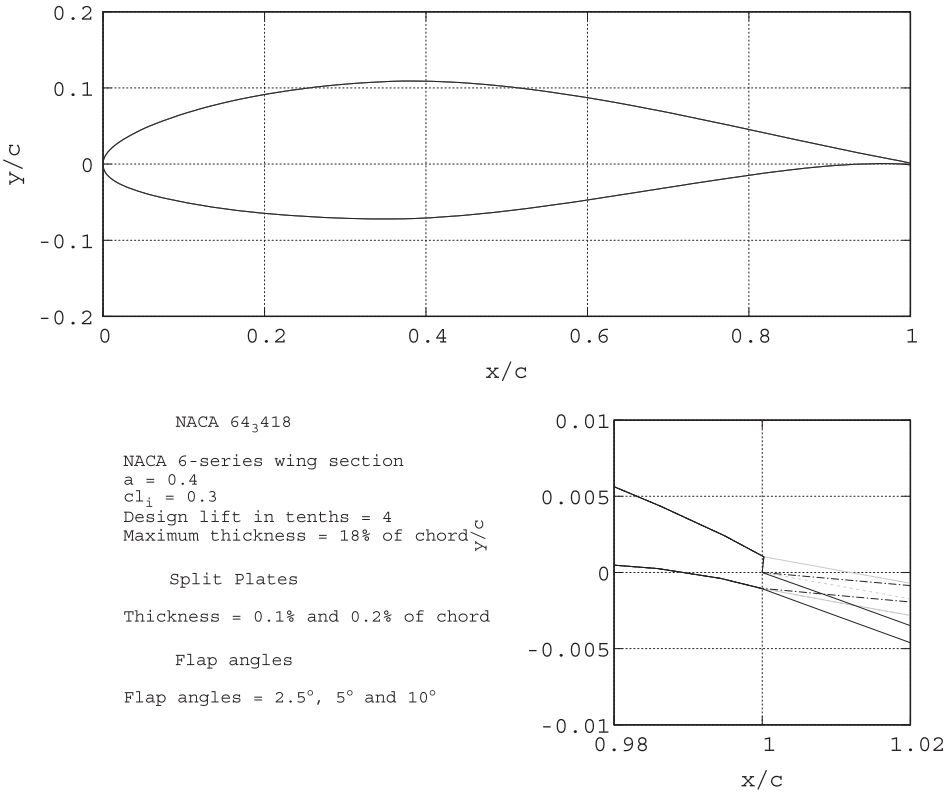

FIGURE 2 NACA 64_3418 original geometry and a detail of the trailing edge extensions

ratio equal to 1. Boundary layer transition has not been forced to a turbulent one but rather left to the effect of the airfoil curvature and pressure gradient. Reference values of ambient pressure equal to a gauge pressure of 0 Pa, density of 1.225 kg/m^3 , and temperature of 288.16 K have been prescribed. With an additional dynamic viscosity of $1.79 \cdot 10^{-5}$ kg/m · s and a wind speed of 44 m/s, a Reynolds number of $3 \cdot 10^6$ has been obtained.

3 | AIRFOIL MESH

The multiblock meshes are generated using ICEM CFD. The particular typology of the mesh allows changing the resolution within the domain, as well as optimizing the number of elements needed for the computation. C-type grids are used for the discretization of both 2D and 3D domains. The domains extend for 10 c upstream and 20 c downstream the airfoil. The quality of the meshes is evaluated with a dedicated ICEM algorithm. The parameter used for the evaluation of the mesh quality is based upon the determinant of the Jacobian matrix of the mesh elements in the domain. In particular, the ratio between the smallest and the largest determinants gives an estimation of the amount of degenerated elements. The presence of degenerated or inverted elements will determine a ratio of 0 or negative, whereas a regular distribution of similar elements will drive the ratio to 1. In all tested configurations, the ratio is kept between 0.7 and 1. As additional verification parameters, the skewness of the mesh elements (following Eriksson model[23]) is monitored and kept within the range 0.7 to 1.

Modeling of the boundary layer is assessed by estimating the nondimensional wall distance of y+ with respect to the airfoil flow at the tested Reynolds number. For these simulations, a y+ with a maximum value of 1 is desirable. Taking into account the incoming flow conditions, for obtaining this value ,the first element of the boundary layer must be located at $y/c = 8.6 \cdot 10^{-6}$ from the wall. A wall function with a growing ratio of 1.2 is applied to increase the spatial resolution from the inner boundary layer size to the one in the outer region. Details of the mesh are presented in Figure 3.

In order to limit the number of computations needed for the study, an analysis of the sensitivity of the mesh to the number of cells has been carried out. The flow around the clean airfoil configuration has been evaluated by using the one-equation Spalart–Allmaras model, while the k-omega SST formulation has been used for the more complex geometry of the airfoil with trailing-edge extensions. The drag coefficient has been chosen as one of the most relevant parameter for monitoring of the convergence of the results because of its sensitivity to transition, separation, and to the fluctuations in the viscous regions of the flow.

Figure 4 shows the results from the sensitivity analysis of the mesh. For the Spalart–Allmaras simulations, the convergence of the solution is monotonically reached with $0.1 \cdot 10^6$ elements, while for the k-omega SST model, corresponding to the NACA64418 with trailing-edge extension, the converged solution has been reached with $0.14 \cdot 10^6$. Richardson extrapolation method[24,25] has been used for analysis of the converged

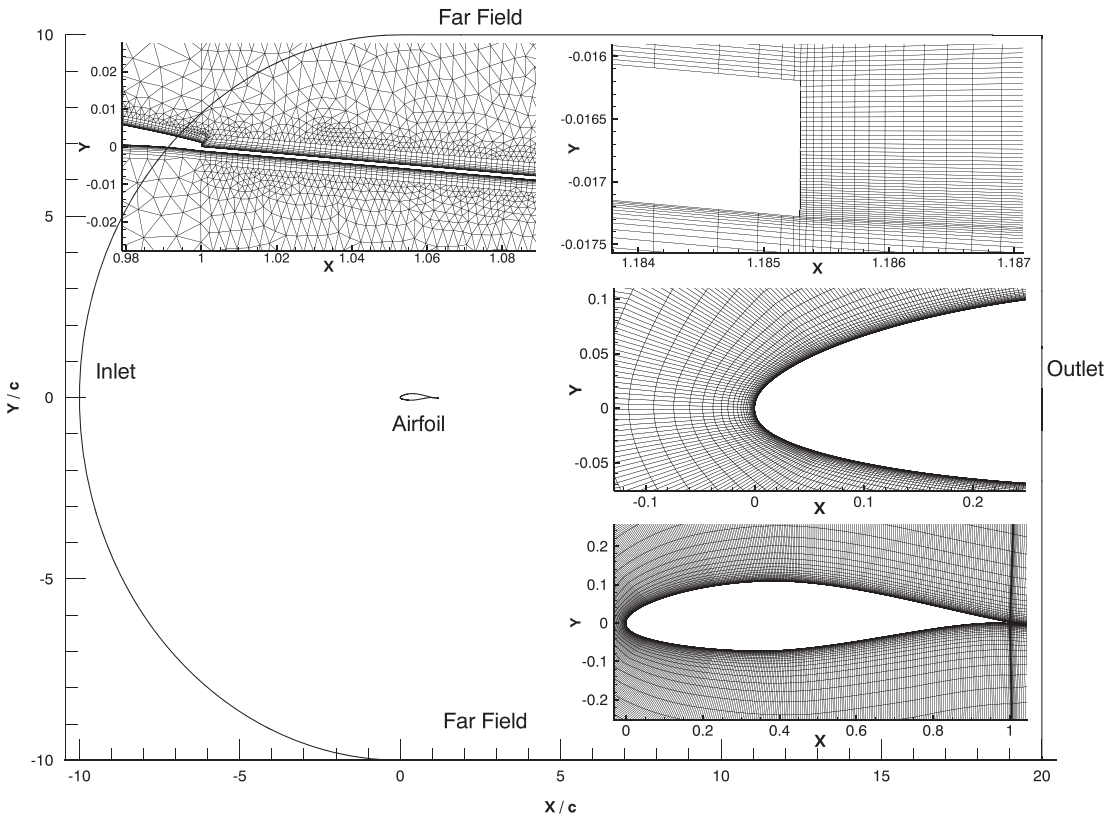

FIGURE 3 Topology of the airfoil mesh and details of the airfoil, the plate end, and the airfoil leading edge, first element sited at $y/c = 8.6 \cdot 10^{-6}$

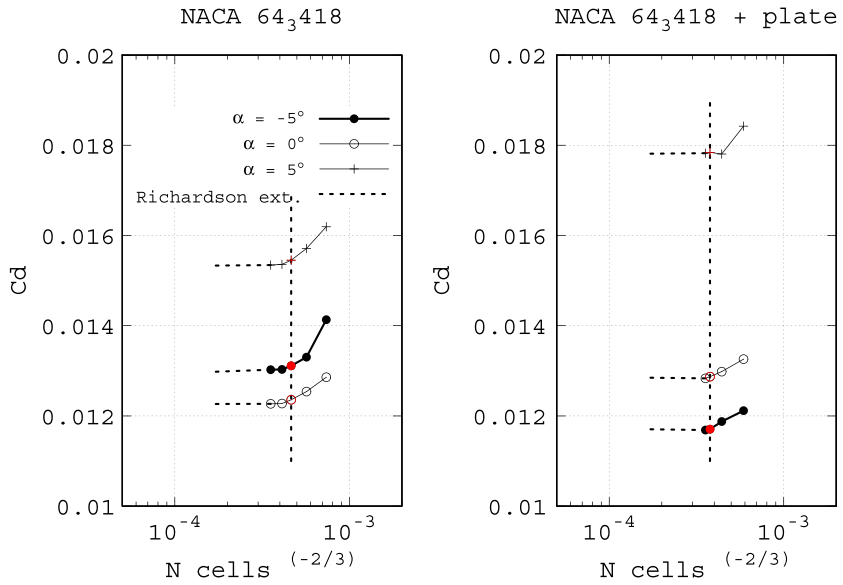

FIGURE 4 Grid sensitivity study for the airfoil using Spalart–Allmaras model and for the airfoil with a trailing edge plate using k-omega SST model. Drag coefficient for different meshes at angles of attack = -5°, 0°, and 5°. The vertical line and the red points show the selected grids [Colour figure can be viewed at wileyonlinelibrary.com]

results. With this methodology, the numerical solution for a given grid, Φ_i, can be calculated as a function of the exact solution, Φ_0, a constant, α, and the observed order of accuracy of the numerical method, p, using the following equation:

$$\Phi_i = \Phi_0 + \alpha \cdot h_i^p. \tag{1}$$

Eça and Hoekstra[26] observed that more than a grid triplet is necessary for carrying out this estimation. In this study, more than four meshes are used for the sensitivity analysis. Comparing the converged drag coefficient obtained with Richardson methodology and the actual mesh values, differences of about 1% were calculated for that specific number of cells, N. Since the different meshes have been obtained by reducing the size of the largest element in the far field and by increasing the number of cells around the airfoil contour and in the boundary layer (keeping constant the y+ element), this entails that a maximum resolution of 40 cells in the boundary layer and 620 in the airfoil contour are sufficient for an accurate representation of the flow field.

All 3D meshes adopted in this study have been consequently obtained by extrusion of the 2D meshes along the z axis. For the airfoil with the trailing edge serrations, a new 3D unstructured mesh has been prepared based on the previous extrusion to adapt to the periodic triangular geometry. This mesh ensures a good boundary layer characterization using a structured mesh near the airfoil contour. In this part, the first element size, the number of layers, and the growing ratio have been fixed. To ensure that the boundary layer is well discretized, the meshes have been obtained by considering a span-wise minimum resolution of $8.6 \cdot 10^{-6}$m corresponding to the flow structures of the size of $y/\lambda = 0.4$ as in the study of Arce et al.[16]

4 | LIFT AND DRAG RESULTS

The change of the aerodynamic performance due to the installation of the trailing-edge serrations is analyzed with respect to the NACA 64$_3$418 with a straight trailing edge. The analysis of the performance features a first comparison of the 2D and 3D simulations. In this respect, the similarities of the serration geometry to a 2D flap are investigated, with the aim of tackling the level of complexity needed to accurately approximate the change in lift and drag of the periodic geometry. The analysis continues with the sensitivity of the turbulence modeling in the 2D and 3D meshes and concludes with the effect of the flap angle of the serration in the airfoil performance.

4.1 | Aerodynamic forces

In this section, the aerodynamic coefficients for the original airfoil, the airfoil with the split plate, and the airfoil with serrated trailing edge extensions are presented. In Figure 5, lift and drag coefficients are shown for the three different turbulence models. It must be noted that for all the simulated cases, the aerodynamic coefficients, lift and drag, are obtained using the chord of the original airfoil without including the length of the plate or serrations. The results of the serrated trailing edge have shown that for all the studied angles of attack, the serrated extensions do not significantly change the lift coefficient of the airfoil, but they cause increased drag coefficient regardless of the turbulence model analyzed.

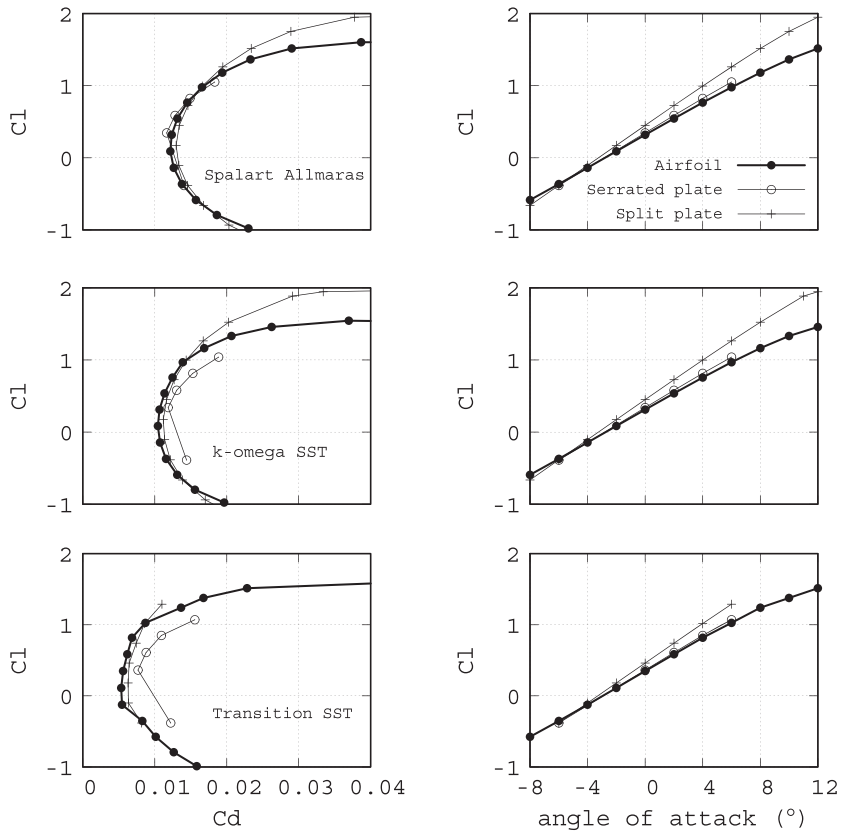

FIGURE 5 Aerodynamic coefficients for the original airfoil, with a split plate and with a serrated trailing edge, for three different turbulence models

On the other side, the split plate originate a lift enlargement caused by the increase in the effective area of the airfoil. The plate significantly affects the lift coefficient over the positive angles of attack.

When comparing the drag coefficient plots in Figure 5, notable differences can be found between the fully turbulent models (Spalart– Allmaras and k-omega SST) and the transitional model (Transition SST). The drag coefficient obtained with the Transition SST model presents lower-drag values because of the more realistic representation of the boundary layer of the airfoil, simulating the natural transition from laminar to turbulent flow. These results are consistent with Menter et al[27]: in this work, it was demonstrated with different experiments that the Transition SST model shows a better agreement with real flows than the fully turbulent models. Different geometries were tested and in all the studied cases, the drag coefficient shows lower values than the fully turbulent models and a very good agreement with the experimental results.

4.2 | Boundary layer

In this section, a comparison of the boundary layer thickness (δ) between the original geometry and the airfoil with a serrated trailing edge is presented. Results are shown for the Transition SST model, however, all tested turbulence models present the same trends. Figure 6 compares the boundary layer thickness of the airfoil, the airfoil with a split plate, and the airfoil with trailing edge serrations in two different positions, the trailing edge suction and pressure side (location 1 of Figure 7). In this figure, it is shown that the boundary layer thickness is modified by the presence of trailing edge extensions, ie, for an angle of attack of 2°, δ/c on the suction side is about 0.0185 on the airfoil, 0.0268 on the airfoil with a split plate, and 0.0205 on the serrated airfoil and on the pressure side is 0.0132 on the airfoil, 0.02214 on the airfoil with a split plate, and 0.013 on the serrated airfoil and for an angle of attack of 6°, δ/c on the suction side is about 0.0272 on the airfoil, 0.0385 on the airfoil with a split plate, and 0.038 on the serrated airfoil and on the pressure side is 0.009 on the airfoil, 0.0174 on the airfoil with a split plate, and 0.0128 on the serrated airfoil.

Comparing the boundary layer thickness at different positions along the teeth just in the suction side (see Figure 7 and Table 1) for an angle of attack of 2°, it is shown that the boundary layer thickness changes slightly from the middle of the teeth to the root in the spanwise direction. Analyzing the distribution of the boundary layer thickness along the teeth length for this cambered airfoil, it is found that on the suction side, this value increases from root to tip. These results show a good agreement with the experimental results carried out by Gruber et al[28]: in this work, a comparison of the boundary layer profiles between the unserrated baseline, and the serrated edge has been displayed for the NACA 65(12)-10 cambered airfoil.

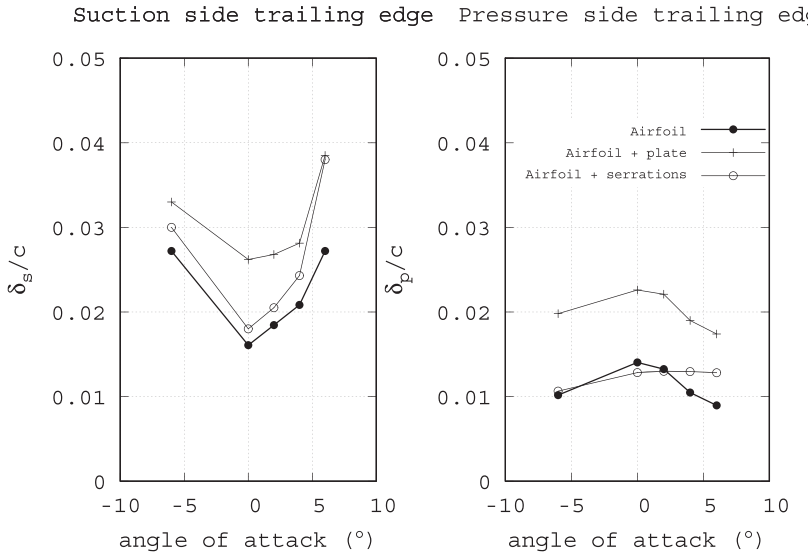

FIGURE 6 Comparison of the nondimensional boundary layer thickness at different angles of attack for the airfoil with and without trailing edge extensions at the airfoil trailing edge on the suction and pressure side for the Transition SST model

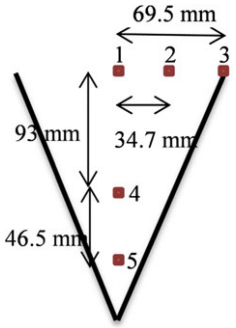

FIGURE 7 Serration scheme with the points in which δ_s/c has been obtained for $\alpha = 2°$ [Colour figure can be viewed at wileyonlinelibrary.com]

TABLE 1 Nondimensional boundary layer thickness

Point	δ_s/c
1	0.0205
2	0.0203
3	0.0195
4	0.021
5	0.023

4.3 | Wake development

An analysis of the flow in the wake of the airfoil, the airfoil with the split plate, and with the trailing edge serrations is presented. As in the previous section, only results for the Transition SST model are displayed.

The wake velocity and turbulent kinetic energy (TKE) profiles for the three studied geometries at $\alpha = 6°$ are shown in Figures 8 and 9. Four downtream locations are analyzed, x = 1.3 c, 1.4 c, 2.2 c, and 3.2 c. It can be observed that the tooth tip and the end of the split plate are located at x = 1.187 c. For the serrated case, two different positions are studied, the tooth tip and the tooth root, for this case, two flow profiles are displayed.

In Figure 8 , it can be observed that the flow at the tip position of the serrated geometry follows similar wake profile to that of the original geometry but with a slightly lower velocity deficit. This means that the tip has a fuller wake compared with the original airfoil. For the case of the split plate, the profile is also similar but with a higher velocity deficit. This higher velocity deficit of the split plate is due to the larger effective chord length. The root flow shows a different behavior from the tip flow, it has a smaller velocity deficit, and the dip location is moved upwards

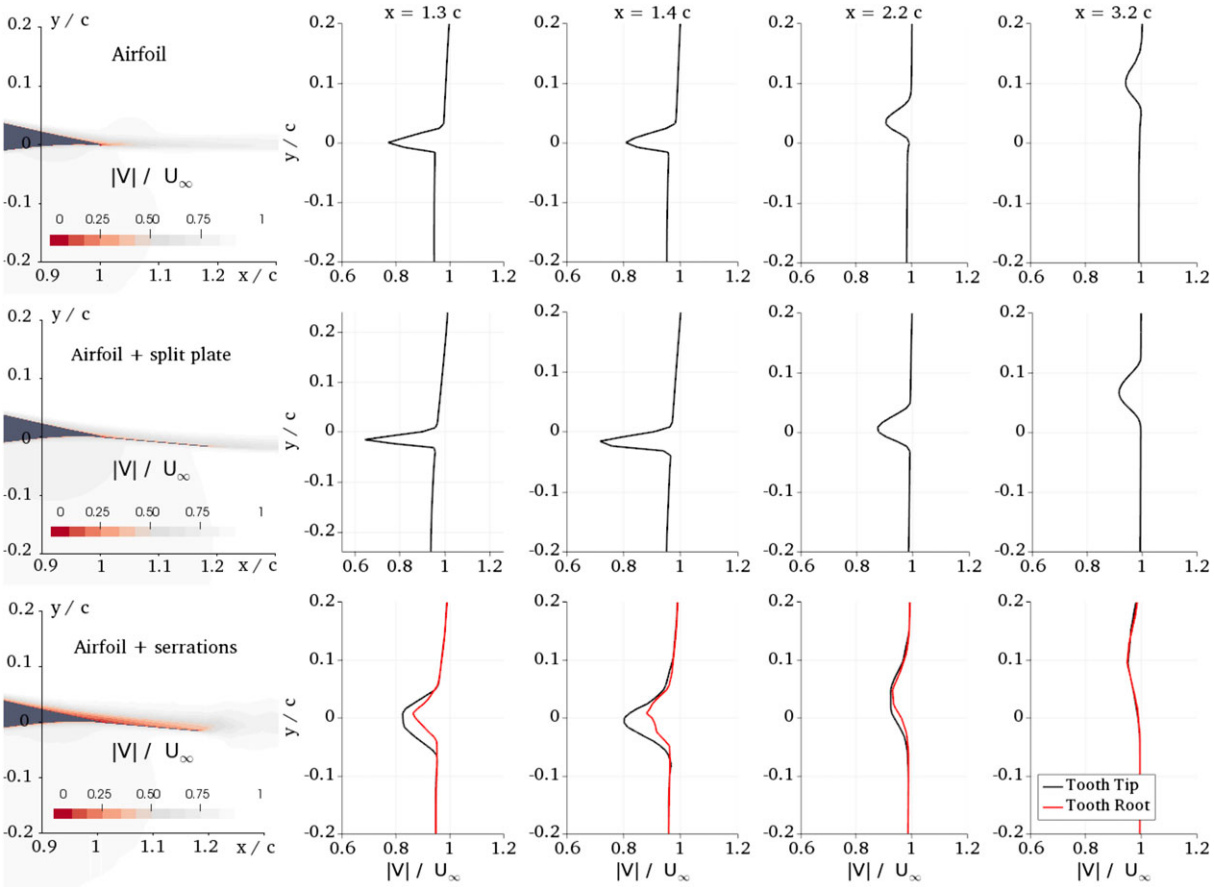

FIGURE 8 Nondimensional velocity magnitude in an X–Y plane for the different studied geometries, nondimensional values of velocity magnitude at different streamwise positions (x = 1.3 c, 1.4 c, 2.2 c and 3.2 c) have been included for the Transition SST model [Colour figure can be viewed at wileyonlinelibrary.com]

because of the flow through the serrations valleys. These differences between the tip and the root flow gradually disappear at far-wake locations. The presence of serrations produces a minor deficit of velocity but an enlargement of this deficit along the y-axis as it is shown in the work of Liu et al.[14]

The wake profiles show different behavior for the case of the serrations and for the case of the plate. These differences are mainly caused for the 3D motion existing between the teeth of the serrations, in the case of the plate, this motion is practically two dimensional. The 3D effects of the flow passing through the serrations and moving from the pressure to the suction side produce a wide and short wake, meanwhile, the plate due to higher effective length origins a narrow and long wake, and its effect is still appearing in x = 3.2 c, but for the serrations case at this position, the velocity deficit has almost disappeared.

The turbulent kinetic energy profiles at different wake locations are displayed in Figure 9. The wake profiles of the original airfoil show the two shear layers originating from combination of the boundary layers on the pressure and suction sides of the airfoil. The effect is more evident for the airfoil with the split plate because of the increase in the effective chord of the airfoil. For the tip and root flow, just a single peak was obtained as the two-boundary layer mix together. A significant different turbulent kinetic energy profile appears for both positions compared with the original airfoil. Lower values and high-TKE dissipation are shown for these locations as a result of a three-dimensional near-wake flow. As in the previous case, the root flow shows an upward moved peak position caused by the flow moving upwards from the serrations valleys. These results shows that the use of serrations produces significant changes on the TKE of the flow, enlarging the high-TKE region along the y-axis and producing a less- turbulent far wake. All these results show a good agreement with the measurements carried out by Liu et al[14] for the NACA 65(12)-10 airfoil.

Results of several cross-flow planes at different locations, x = 1.005 c (root tooth), x = 1.093 c (middle tooth), and x = 1.187 c (tip tooth) are presented in Figure 10, where the streamwise vorticity component, w_x, for the serrated geometry at an angle of attack of 6° is displayed. As in the previous part, the results represented correspond to the Transition SST model. The presence of streamwise vortex pairs emanating from the serrations is evident from these results. Strong variations between negative and positive streamwise vorticities are shown between the teeth resulting from the pressure differences between the two sides of the serrations, and these results coincide with the experimental data from Arce et al[16]: in this study, vortex pairs generated between the teeth that produce a vigorous motion are measured. Other studies like the one of Jones et al[18] have shown that in the presence of serrations, the flow is highly three dimensional, they reported the formation of horseshoe vortices in the space between serrations, exacerbated by the presence of a mean flow motion through the serrations from the suction to the pressure

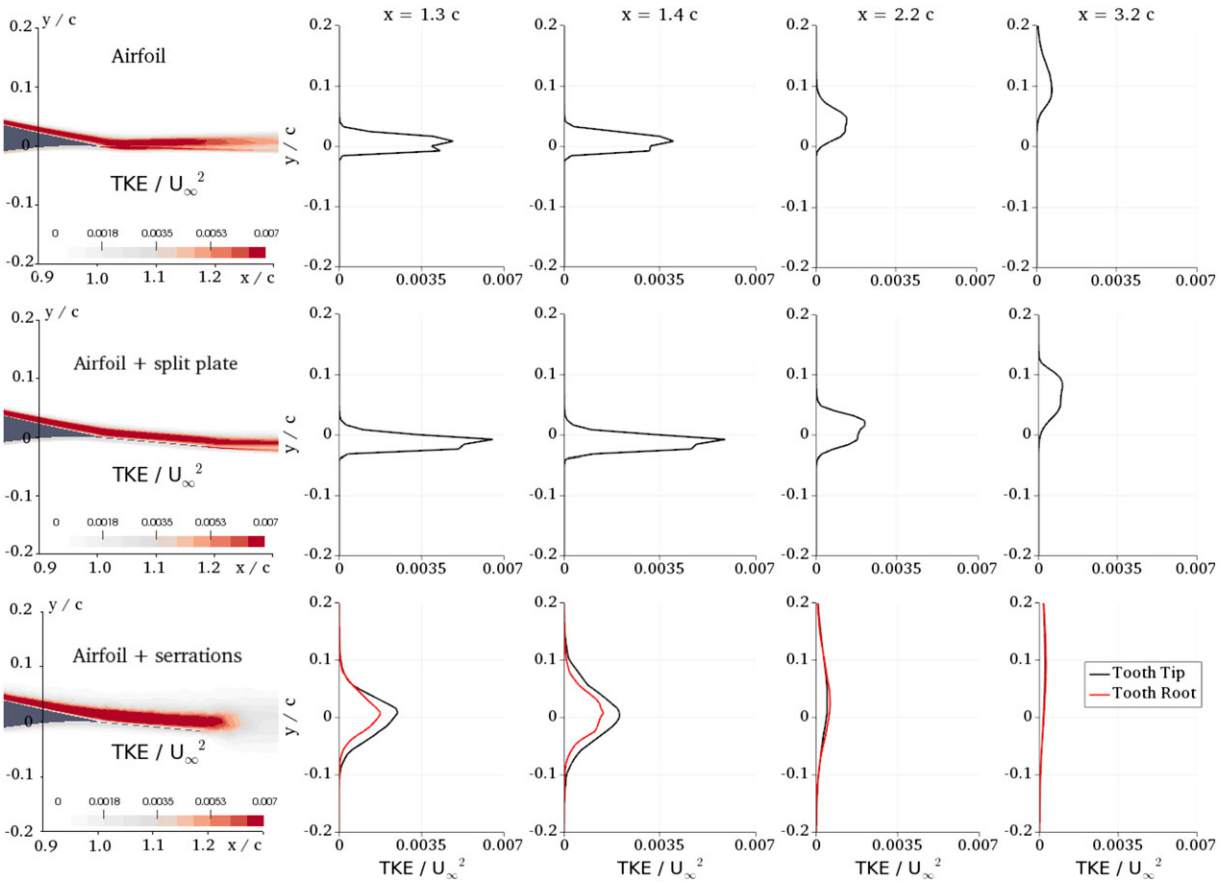

FIGURE 9 Nondimensional TKE in an X–Y plane for the different studied geometries, non-dimensional values of TKE at different streamwise positions (x = 1.3 c, 1.4 c, 2.2 c and 3.2 c) have been included for the Transition SST model [Colour figure can be viewed at wileyonlinelibrary.com]

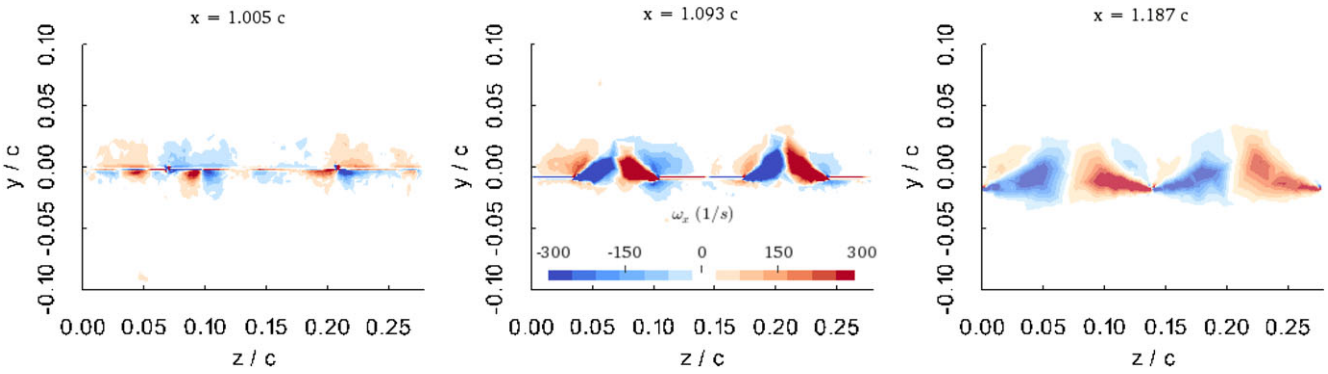

FIGURE 10 Streamwise vorticity component in a Y–Z plane at different locations for the Transition SST model [Colour figure can be viewed at wileyonlinelibrary.com]

side. These three-dimensional structures are generated at the root of the teeth, at the middle of the teeth (x = 1.093 c), the structures are fully formed, and they dissipate in the wake.

4.4 | 2D model of lift and drag changes

In order to obtain a simplified model that can be easily extended to several airfoil shapes, a comparison of the 2D airfoil performance with the ones obtained from the full 3D test cases is carried out. Experimental data from Abbott and von Doenhoff[19] and additional numerical data from XFOIL[29] are used to consolidate the study. In particular, a first analysis of the lift and drag performance of the clean NACA airfoil is carried out in Figure 11, where the experimental lift and drag coefficients obtained from Abbott and von Doenhoff[19] are directly compared with the ones obtained from XFOIL. The best agreement with the experimental results at the $Re_c = 3 \cdot 10^6$ is obtained by imposing a free transition model with a $N_{crit} = 9$ in XFOIL. Figure 11 shows a relatively good agreement between the experimental and the numerical data for this particular airfoil, allowing using XFOIL for a more extended comparison with different angles of attack and with serrations. Because of the particular conformal

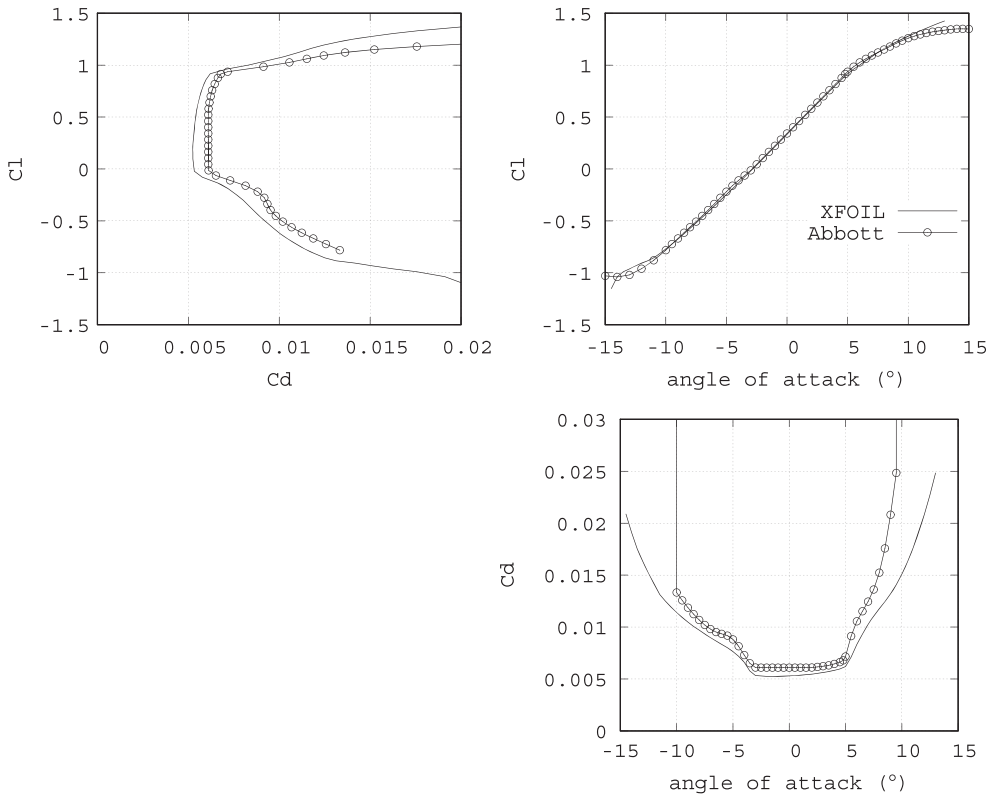

FIGURE 11 Comparison between XFOIL and experimental results from Abbott and von Doenhoff for the airfoil without any trailing edge extension at a $Re_c = 3 \cdot 10^6$

transformation that generate the NACA six-series airfoil, typically about 50% of the entire airfoil is covered with laminar flow at relatively high Reynolds. This allows the creation of the low-drag region that can be appreciated in Figure 11. Although retaining optimal drag characteristics for a large range of angles of attack, the transition from laminar to turbulent flow is abrupt (at a Cl of about 1). This effect is generally ascribed to the vicinity of the pressure minimum of the airfoil to the transition point. The presence of a slight overprediction of the maximum lift coefficient as well as an underprediction of the drag coefficient (for all angles of attack) is a common disagreement derived from the nonexact boundary layer representation between XFOIL and experimental results.[30] This last underestimation of the drag coefficient in the prestall regime has been often reported as a main mismatch of the skin friction coefficient of the airfoil surface. Nevertheless, the main features corresponding to the drag coefficient change due to transition and separation, the linear region of the lift coefficient in prestall conditions, and the cambered asymmetry of the flow is well represented by XFOIL in comparison with the experimental data available from literature, allowing using the software for validating the CFD simulations in the remainder section.

Figure 12 represents the computational Cl-Cd and the lift coefficient versus angle of attack curves pertaining to the turbulence model Transition SST. In the same graphs, the results from the NACA 64_3418 with a split plate and with the serrated geometry are compared. It has to be noted that a 3D computation of the airfoil with a split plate at the trailing edge has additionally been carried out. Since the results have been found almost exactly the same as for its 2D counterpart (due to the two-dimensionality of the flow), that simulation has not been included in the manuscript. In this figure, results from XFOIL have been included for validating the CFD case of the airfoil with a split plate. It is important to remark that for all the simulated cases, the lift and drag coefficients are calculated using the chord of the original airfoil without including the length of the plate or serrations.

From analysis of Figure 12, the main change of performance given by the serrated configuration with respect to a split plate consist of a change of

- slope of the lift coefficient and
- drag profile location.

From the results obtained it can be assumed that the serration behave as a reduced flap of lower area. The change in slope of the lift coefficient is indeed consistent with a finite extension of the airfoil camber proportional to the length of the serration. Such extension can also represent the finite increase in drag due to the larger airfoil sectional area (ie, equivalent thickness per unit chord) seen by the flow. The same differences between the 2D and 3D simulations have been appreciated for all turbulence models. Once adopting linear thin airfoil theory (TAT),[31] the relation between the airfoil lift without add-ons (Cl_a) and the one with installation of the split-plate (Cl_{ap}) can be formalized by the following equations:

$$Cl_a = 2\pi\alpha + Cl_0 \tag{2}$$

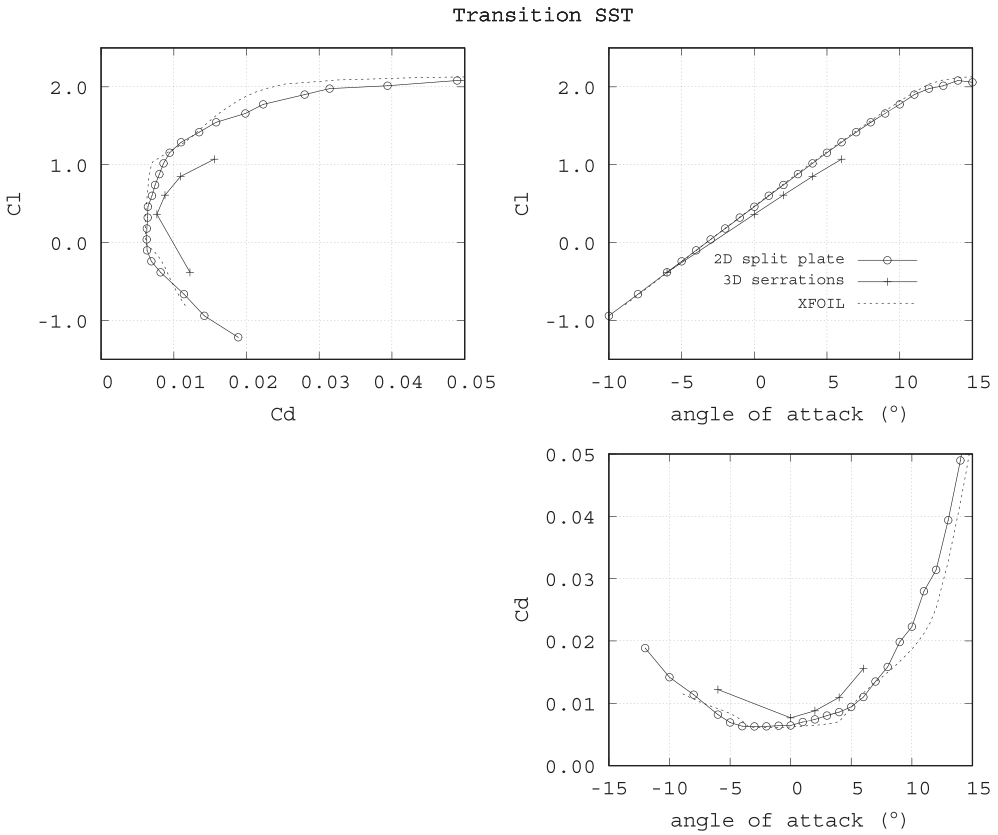

FIGURE 12 Aerodynamic information of the 2D NACA 64_3418 with a split plate, 3D NACA 64_3418 with serrations both for the Transition SST model and XFOIL simulations for the NACA 64_3418 with a split plate

$$Cl_{ap} = 2\pi\alpha(1 + l/c) + 2\pi\beta l/c + Cl_0, \tag{3}$$

where the lift coefficient is obtained as a function of the angle of attack α, the flap angle β, the chord c, and the plate length l. For validating this equation, a comparison between experimental data obtained from Abbott and von Doenhoff[19] and results obtained from the previous equation is presented. In Figure 13, the lift coefficient of different NACA airfoils with a flap length of 0.2 c and a flap angle of 60° is compared. In these graphs, a good approximation of the lift coefficient for all the cases is presented.

Once the validity of the Equation 3 is proved using experimental data, the same methodology for obtaining the lift coefficient for the airfoil with serrations Cl_{as} can be applied.

$$Cl_{as} = 2\pi\alpha(1 + l_s/c) + 2\pi\beta l_s/c + Cl_0 \tag{4}$$

With Equation 4, it is possible to obtain an accurate estimation of the lift coefficient of an airfoil with serrations from the 2D results of the airfoil with a split plate. For this purpose, a relation between the equivalent serration length and the plate length must be obtained. In Figure 14, different lift coefficients calculated using Equation 4 with different equivalent serrations lengths have been compared with the CFD simulations. Focus on the angles of attack ranging from 0° to 6° in which the TAT is more precise, it is clear that a reduced serrated length shows a better agreement than the equivalent serrated area ($l_s = 1/2 \cdot l$). Looking into Figure 14, it can be concluded that $l_s = 1/8 \cdot l$ is an adequate approximation for calculating the serrated lift coefficient from the split plate data, although more simulations are recommended to extend its validity to other airfoils and flap angles.

4.5 | Effect of the turbulence modeling in the serration flow

In the previous section, a comparison of the 3D serrated airfoil and a 2D simplification was carried out. Although the performance results seem to be rather similar with different turbulence models, previous studies have shown significant variations when comparing different computational RANS-based methods for airfoil flows.[32] In Figure 15, the polar data for the 3D serrated airfoil and for the 2D simplification are shown for each turbulence model.

The lift coefficient is almost the same for the three turbulence models, the drag coefficient instead shows larger deviations especially when comparing the Spalart–Allmaras and k-omega SST models (as in the previous sections, the lift and drag coefficients have been obtained using the chord of the original airfoil without including the length of the plate or the serrations). More representative of the actual flow behavior is the

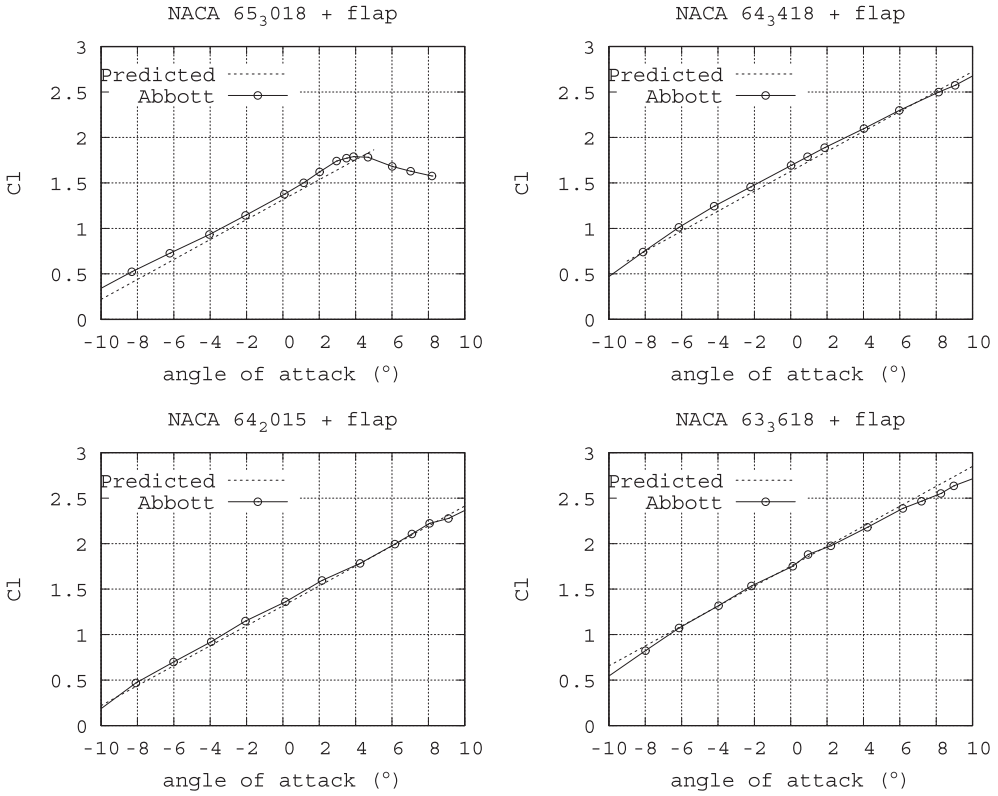

FIGURE 13 Lift coefficient comparison between predicted and experimental data for different NACA six-digit airfoils

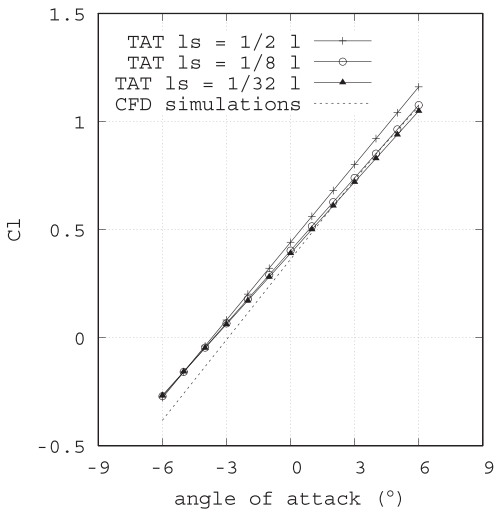

FIGURE 14 Lift coefficient for the NACA 64_3418 with serrations obtained from the thin airfoil theory with different serrations lengths and from 3D CFD simulations

Transition SST model, due to its intrinsic modeling of the laminar to turbulent transition of the boundary layer. While indeed the first two models are modeling a fully turbulent flow at the current cell resolution, the last one simulates more accurately the boundary layer characteristics of the airfoil in the linear angle of attack regime. It has to be noted that the Spalart–Allmaras model shows rather larger differences in the case of the airfoil with a split plate, but these differences are smaller in the case of the serrated airfoil, the reason of this variance is the lower accuracy in the prediction of the boundary layer size.

4.6 | Influence of the flap angle

The effect of the mounting angle of the serration is here studied as a change of the flap angle of the geometry, angle between the serration/split-plate geometry and the chord of the airfoil (β). Three flap angles have been simulated for the present test case, namely, 2.5°, 5°, and 10°. For this analysis, TAT has been used as in the previous section. With this theory, the lift coefficient for the airfoil with serrations mounted

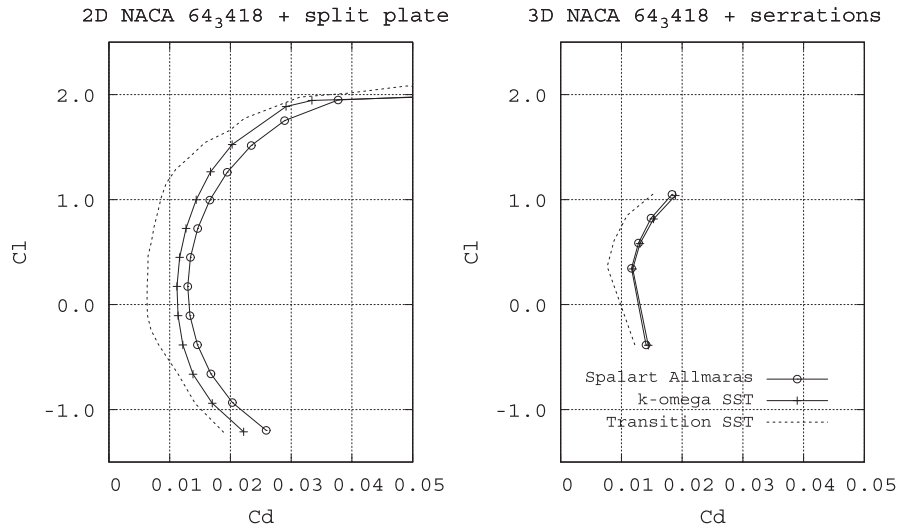

FIGURE 15 Aerodynamic information of the 2D NACA 64$_3$418 with a split plate and 3D NACA 64$_3$418 with serrations for the three turbulence models

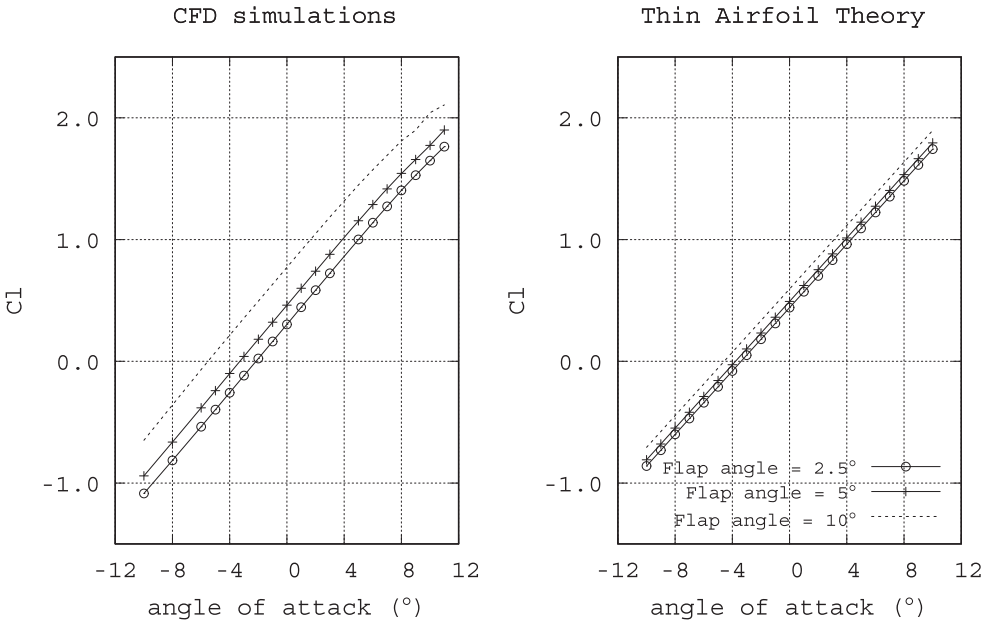

FIGURE 16 Lift coefficient of the NACA 64$_3$418 with a split plate mounted at different flap angles obtained with the thin airfoil theory and with CFD simulations

at different flap angles can be predicted following Equation 4. In this formula, an increase in the flap angle produces an upward displacement of the lift curve maintaining the same $Cl - \alpha$ slope.

In Figure 16, the lift coefficient for the airfoil with a split plate mounted at different flap angles obtained with the TAT and with CFD simulations has been displayed (the lift coefficient has been calculated using the chord of the original airfoil without taking into account the length of the plate). In this case, the same tendency is shown for both methods, but larger differences are presented for the CFD simulations. These differences between methods might be caused by the simplifications made by the TAT. Higher differences in lift coefficient are expected from the CFD simulations regardless of the turbulence model used.

Regarding the drag coefficient, only CFD simulations are presented because the TAT predicts zero drag force. As in the previous case, the results are independent of the turbulence model. The same trend is observed in the Spalart–Allmaras, the k-omega SST, and the Transition SST models. Focus on the Transition SST model, which is the most similar to reality, the drag coefficient curve for each flap angle has the same shape but shifted along the angle of attack. In Figure 17, the drag coefficient for the different flap angles are displayed.

With this information, it is clear that there is a relation between the aerodynamic performance of the airfoil with serrations mounted at different flap angles. It is possible to obtain the lift coefficient for different flap angles without repeating the CFD simulations using the Equation 4 based on the TAT. This relation is dependent on the length, shape, and flap angle of the serrations so for extrapolating the results to other geometries, more simulations should be done.

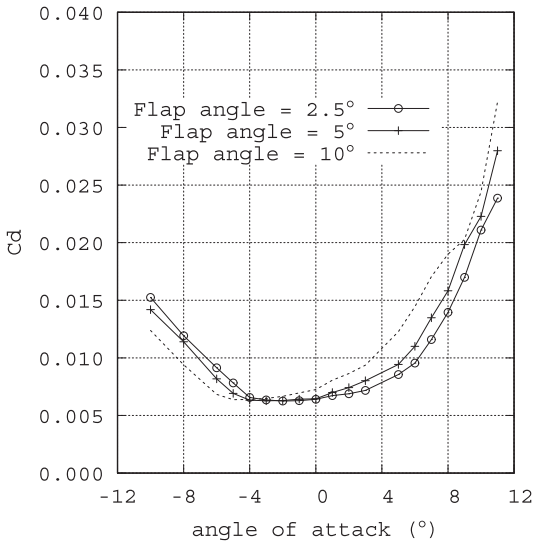

FIGURE 17 Drag coefficient of the NACA 64_3418 with a split plate mounted at different flap angles obtained from CFD simulations (Transition SST model)

5 | CONCLUSIONS

A theoretical study on the NACA 64_3618 airfoil with serrated trailing edge extensions have been carried out to analyze the impact of these devices on the aerodynamic performance of the original airfoil geometry. For this analysis, 2D and 3D RANS simulations using different turbulence models have been performed. From these simulations, a prediction law for the lift coefficient of the airfoil with serrated trailing edge extensions has been derived. With this equation, the lift coefficient of the serrated airfoil can be easily predicted. The aerodynamic forces of the airfoil have been obtained from the simulations. Results show that the addition of trailing edge serrations changes significantly the aerodynamic performance of the airfoil. Although slightly changes are observed on the lift coefficient, the drag coefficient is increased for the presence of the serrations. The velocity profiles are also modified, and notable differences are observed between the flow on the root and tip position, showing an upwards displacement of the dip position of the root flow due to the movement of the flow through the serrations valley. The analysis of the cross-flow plane shows the presence of streamwise vortices emanating from the serrated edge. This three-dimensional flow and vortices influence the turbulent energy decay at the wake region bringing down the turbulence level significantly compared with the original airfoil.

The analysis of the turbulence effect in the serrations flow has also been investigated. From this work, it is demonstrated that the impact of the different turbulence models used are limited to the drag coefficient. The transition model shows lower-drag coefficient than the fully turbulent because of the better modeling of the boundary layer flow, including the natural transition from laminar to turbulent. This more accurate representation of the boundary layer allows for lower-drag values more similar to the experimental results than the fully turbulent. This study is complimented with the analysis of the flap angle influence on the aerodynamic forces over the airfoil. The effect of this mounting angle on the lift coefficient can be predicted with a derived law that shows and increment of the lift values as the flap angle is augmented.

ORCID

Elena Llorente http://orcid.org/0000-0001-7759-2241
Daniele Ragni http://orcid.org/0000-0002-8014-5650

REFERENCES

1. Berg F, Pedersen E, Bouma J, Bakker R. Project windfarmperception visual and acoustic impact of wind turbine farms on residents, University of Groningen; 2008.
2. Wagner G. *Wind Turbine Noise*. Berlin, Heidelberg: Springer; 1996.
3. Howe MS. A review of the theory of trailing edge noise. *J Sound Vib*. 1978;61(3):437-465. https://doi.org/10.1016/0022-460X(78)90391-7
4. Dassen T, Guidati G, Wagner S, Kang S, Parchen R, Khodak A. Comparison of measured and predicted airfoil self-noise with application to wind turbine noise reduction. NLR-TP-97564; 1997.
5. Moreau DJ, Doolan CJ. Noise-reduction mechanism of a flat-plate serrated trailing edge. *AIAA J*. 2013;51(10):2513-2522. https://doi.org/10.2514/1.J052436
6. Lyu B, Azarpeyvand M, Sinayoko S. Prediction of noise from serrated trailing-edges. *J Fluid Mech*. 2015;793:556-588. https://doi.org/10.1017/jfm.2016.132
7. Gruber M, Joseph P, Chong T. On the mechanisms of serrated airfoil trailing edge noise reduction. In: American Institute of Aeronautics and Astronautics; Portland, Oregon. 2011:2781.

8. Oerlemans S, Fisher M, Maeder T, Kögler K. Reduction of wind turbine noise using optimized airfoils and trailing-edge serrations. *AIAA J*. 2009;47(6):1470-1481. http://arc.aiaa.org/doi/abs/10.2514/1.38888
9. Jaworski JW, Peake N. Aerodynamic noise from a poroelastic edge with implications for the silent flight of owls. *J Fluid Mech*. 2013;723:456-479. https://doi.org/10.1017/jfm.2013.139
10. Vathylakis A, Chong TP, Joseph PF. Poro-serrated trailing-edge devices for airfoil self-noise reduction. *AIAA J*. 2015;53(11):3379-3394. https://doi.org/10.2514/1.J053983
11. Herr M. Design criteria for low-noise trailing-edges. In: American Institute of Aeronautics and Astronautics. Rome, Italy; 2007:3470.
12. GAMESABrochure G114-2.0MW; 2016.
13. SIEMENSBrochure SWT-4.0-130; 2015.
14. Liu X, Jawahar HK, Azarpeyvand M, Theunissen R. Wake development of airfoils with serrated trailing edges. In: American Institute of Aeronautics and Astronautics (AIAA). Lyon, France; 2016:2817.
15. Avallone F, Leon CA, Pröbsting S, Lynch KP, Ragni D. Tomographic-PIV investigation of the flow over serrated trailing-edges. In: American Institute of Aeronautics and Astronautics (AIAA). San Diego, California; 2016:1012.
16. León CA, Ragni D, Pröbsting S, Scarano F, Madsen J. Flow topology and acoustic emissions of trailing edge serrations at incidence. *Exp Fluids*. 2016;57(5). https://doi.org/10.1007/s00348-016-2181-1
17. Chong TP, Vathylakis A. On the aeroacoustic and flow structures developed on a flat plate with a serrated sawtooth trailing edge. *J Sound Vib*. 2015;354:65-90. https://doi.org/10.1016/j.jsv.2015.05.019
18. Jones LE, Sandberg RD. Acoustic and hydrodynamic analysis of the flow around an aerofoil with trailing-edge serrations. *J Fluid Mech*. 2012;706:295-322. https://doi.org/10.1017/jfm.2012.254
19. Abbott IH, von Doenhoff AE. *Theory of Wing Sections*. New York: DOVER PUBLICATIONS, INC.; 1959.
20. Spalart P, Allmaras S. A one-equation turbulence model for aerodynamic flows. In: American Institute of Aeronautics and Astronautics. Reno, Nevada; 1992:439.
21. Menter F. Zonal two equation k-w turbulence models for aerodynamic flows. In: American Institute of Aeronautics and Astronautics. Orlando, Florida; 1993:2906.
22. Menter FR, Langtry RB, Likki SR, Suzen YB, Huang PG, Völker S. A correlation-based transition model using local variables–part i: Model formulation. *J Turbomach*. 2004;128(3):413-422. https://doi.org/10.1115/1.2184352
23. ANSYS. ANSYS FLUENT Help Manual. Ansys; 2016.
24. Richardson LF, Gaunt JA. The deferred approach to the limit. part i. single lattice. part ii. interpenetrating lattices. *Philosophical Transactions of the Royal Society of London A: Mathematical, Physical and Engineering Sciences*. 1927;226(636-646):299-361. https://doi.org/10.1098/rsta.1927.0008
25. Iranzo A, Valle J, Trejo I, Domingo J. An uncertainty estimation example for backward facing step cfd simulations; 2006.
26. Eca L, Hoekstra M. A procedure for the estimation of the numerical uncertainty of cfd calculations based on grid refinement studies. *J Comput Phys*. 2014;262(Supplement C):104-130. https://doi.org/10.1016/j.jcp.2014.01.006
27. Menter FR, Langtry R, Völker S. Transition modelling for general purpose cfd codes. *Flow, Turbul Combust*. 2006;77(1):277-303. https://doi.org/10.1007/s10494-006-9047-1
28. Gruber M, Joseph P, Chong TP. Experimental investigation of airfoil self noise and turbulent wake reduction by the use of trailing edge serrations. *AIAA J*. Stockholm, Sweden; 2010. https://doi.org/10.2514/6.2010-3803
29. Drela M. *XFOIL: An Analysis and Design System for Low Reynolds Number Airfoils*. Berlin, Heidelberg: Springer Nature; 1989.
30. Eisele O, Pechlivanoglou G. Single and multi-element airfoil performance simulation study and wind tunnel validation. *Wind Energy - Impact of Turbulence*. Berlin, Heidelberg: Springer Berlin Heidelberg; 2014:17-22.
31. Anderson J. *Fundamentals of Aerodynamics*. New York: McGraw-Hill Education; 2010.
32. Fernandes GC, Sandberg RD, Weinmann M. Applicability of rans models for accurate computation of flow over airfoils with serrated trailing edges. In: V European Conference on Computational Fluid Dynamics (ECCOMAS CFD). Lisbon, Portugal; 2010:2817.

How to cite this article: Llorente E, Ragni D. Trailing edge serrations effects on the aerodynamic performance of a NACA 64_3418. *Wind Energy*. 2019;22:392–406. https://doi.org/10.1002/we.2293